Three-Phase Relative Permeability and Capillary Pressure Models With Hysteresis and Compositional Consistency

Sajjad S. Neshat and **Gary A. Pope,** University of Texas at Austin

Summary

New coupled three-phase hysteretic relative permeability and capillary pressure models have been developed and tested for use in compositional reservoir simulators. The new formulation incorporates hysteresis and compositional consistency for both capillary pressure and relative permeability. This approach is completely unaffected by phase flipping and misidentification, which commonly occur in compositional simulations. Instead of using phase labels (gas/oil/solvent/aqueous) to define hysteretic relative permeability and capillary pressure parameters, the parameters are continuously interpolated between reference values using the Gibbs free energy (GFE) of each phase at each timestep. Models that are independent of phase labels have many advantages in terms of both numerical stability and physical consistency. The models integrate and unify relevant physical parameters, including hysteresis and trapping number, into one rigorous algorithm with a minimum number of parameters for application in numerical reservoir simulators. The robustness of the new models is demonstrated with simulations of the miscible water-alternating-gas (WAG) process and solvent stimulation to remove condensate and/or water blocks in both conventional and unconventional formations.

Introduction

Relative permeability has been studied for many years because of its importance in the modeling of oil/gas-recovery processes and other applications (Muskat 1949; Baker 1988). Traditional models rely on phase labels to define relative permeability parameters, such as endpoints and residual saturations, and assume no dependence on phase composition. In compositional simulators using traditional models, the phase labels sometimes change from one timestep to another timestep in the same gridblock for the same physical phase. This is called phase flipping. Phase flipping causes discontinuities in the relative permeability and flux calculations. The resulting discontinuities cause numerical oscillations and instabilities, increase the computational time because of smaller timesteps, and are physically incorrect. An example simulation is shown in the Simulation Results section.

The effect of fluid composition on relative permeability has been studied by many authors both experimentally and numerically. Jordan (2016) completed experiments under rigorous conditions at reservoir pressure and temperature to investigate the effect of gas composition on relative permeability in two-phase displacement. He observed a difference in the relative permeability of different fluids [nitrogen (N_2) gas/brine and carbon dioxide (CO_2) gas/brine] in the same core under the same conditions. The new data of Jordan (2016) are consistent with the N_2 gas data reported by Oak et al. (1990) and the CO_2 gas data reported by Dria et al. (1993) and Chen (2016), but these investigators did not make direct comparisons between the relative permeability values of different fluids in the same core. Kalla et al. (2015) found a noticeable difference between the relative permeability of the reservoir and the model gas/condensate mixtures with different compositions but the same interfacial tension (IFT). These experimental studies suggest that it is important to account for the effect of fluid composition on the relative permeability.

Jerauld (1997), Blunt (2000), and Fayers et al. (2000) were among the first authors to recognize the need for at least some limited dependence on composition in a consistent relative permeability model. They used density to interpolate between the oil and gas relative permeability near critical states. This ensures continuity of the relative permeability as a function of composition as it changes between gas-like and oil-like behavior. Yuan and Pope (2012) used the molar GFE of each phase to interpolate the relative permeability parameters between reference values as an alternative to assigning phase labels. They show that the GFE approach guarantees the continuity of the relative permeability curves. Although they recognized the importance of hysteresis, they did not include it in their model. Alzayer et al. (2016) also used the GFE approach for simulation of miscible displacements but did not include hysteresis in their model. They showed that including compositional dependencies in the relative permeability near the critical point affects the numerical results, with significant improvements in nonlinear convergence.

In multiphase flow, hysteresis is modeled through dependence of the relative permeability and capillary pressure on a displacement path. The procedure is relatively straightforward in two-phase flow in which the saturation change is restricted to two directions (i.e., increasing or decreasing) and the saturation path is known (Land 1968; Carlson 1981; Braun and Holland 1995). Modeling of hysteresis in three-phase flow is significantly more challenging, partly because of additional degrees of freedom in the saturation direction. This allows for a total of 12 possible combinations of increasing, decreasing, or constant directions for three-phase saturation and unlimited saturation trajectories defined by two independent saturation values (Larsen and Skauge 1998; Beygi et al. 2015).

The choice of the capillary pressure model and its compatibility with the relative permeability model is also important. Relative permeability is closely related physically to capillary pressure. Therefore, ensuring consistency between physical features such as hysteresis and compositional dependence is a desirable but seldom enforced feature in commonly applied models. In addition, most of the capillary pressure models are only applicable for a specific wettability condition and cannot be used for general cases, including mixed-wetting conditions.

This review accentuates the essential need of developing novel tools for a better description of multiphase-flow problems. New approaches are needed to overcome the limitations of existing models so predictions will be closer to reality. At the same time, the models should be as simple and easy to use as possible, consistent with this need. In particular, the number of parameters in the models should be as small as possible so that it is feasible to estimate these parameters from limited and uncertain experimental data.

Copyright © 2018 Society of Petroleum Engineers

Original SPE manuscript received for review 6 November 2017. Revised manuscript received for review 16 May 2018. Paper (SPE 191384) peer approved 23 May 2018.

This paper presents new models for three-phase relative permeability and capillary pressure for use in compositional reservoir simulators. The new formulation incorporates hysteresis and compositional consistency for both capillary pressure and relative permeability using a minimum number of input parameters. Unlike the traditional models, the proposed GFE approach is not affected by phase flipping and misidentification. The robustness of the model is illustrated with numerical simulations of practical problems involving complex phase behavior.

Three-Phase Relative Permeability Model

Relative permeability in general is a function of saturation, saturation history, and composition. In this study, a Corey equation was used to model the dependence of relative permeability on saturation because of its simplicity and because it is known to be a well-behaved function. However, the same approach used in the new GFE model described in this paper is general so that it can be applied to any type of relative permeability function (Beygi et al. 2015). The Corey model used here is similar to the Brooks and Corey (1966) expression, but developed for a wider range of rock and wettability characteristics. The endpoints, exponents, and residual saturations in the Corey et al. (1956) model can be adjusted to fit specific relative permeability data. The Corey equation is

$$k_{rj} = k_{rj}^{0}\left(\frac{S_j - S_{rj}}{1 - \ S_{ri} - S_{rk}}\right)^{n_j}. \quad (1)$$

During injection of CO_2 in tertiary-recovery processes, a second liquid phase rich with CO_2 often forms at low temperature. In most practical cases, only three phases flow in a typical single gridblock. However, the fourth phase can still affect the relative permeability, because it occupies pore space even when it is not mobile. In this case, a more-general form of Eq. 1 can be used by including the residual saturation of the fourth phase in the denominator.

Approach to Phase Identification and Parameter Calculation. The relative permeability parameters in Eq. 1 (i.e., endpoints, residual saturations, and exponents) are phase-dependent variables. In the proposed model, different hydrocarbon phases are only identified by their molar GFE instead of phase labels and, as a result, all relative permeability parameters are estimated as continuous functions of GFE, as illustrated in **Fig. 1.** This approach offers significant advantages over conventional three-phase models. First, it ensures continuity in the calculated values of the relative permeability and capillary pressure as phases appear or disappear during compositional simulation. Second, relative permeability and capillary pressure parameters are evaluated independent of phase labels, and thus are not affected by phase misidentification or flipping. Third, the GFE model can capture the effect of composition on relative permeability parameters consistent with experimental data.

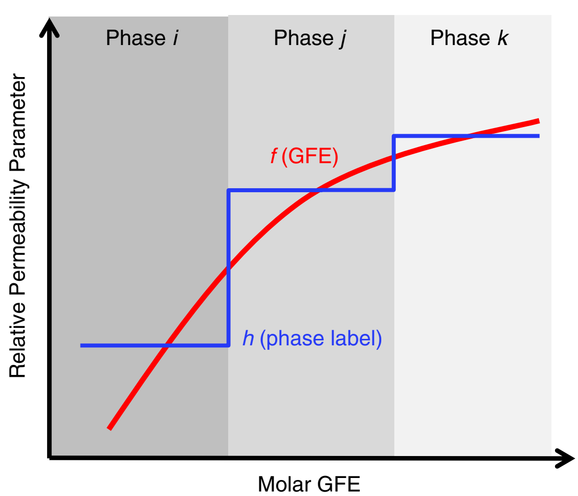

Fig. 1—Schematic of relative permeability parameters as (a) the continuous function *f* of the molar GFE and (b) the discontinuous function *h* of the phase labels.

The functional dependence of relative permeability is not known in general and is difficult to derive from first principles. One simple option is to assume a linear function to interpolate between reference values. This method requires the values of the relative permeability parameters at reference states, which in turn should be dependent on experimental data. The reference states must be set wide enough so that all interpolation that is performed during a simulation falls within these limits. This can be accomplished by simply running each particular simulation to determine the extremes of the GFE.

At constant reservoir temperature, molar GFE is a function of phase composition and pressure and is calculated using

$$\frac{G_j}{RT} = \sum_{n=1}^{n=n_c}\left(x_{nj}\ln\frac{P}{P_R}\right) + \sum_{n=1}^{n=n_c} x_{nj}\ln(x_{nj}) + \sum_{n=1}^{n=n_c} x_{nj}\ln(\phi_{nj}). \quad (2)$$

Fig. 2 shows the profiles of molar GFE and interpolated relative permeability endpoints of oil, gas, and aqueous phases in a mixture of C_1, C_6, CO_2, and water (H_2O) at 260°F during pressure change from dew to bubble pressures at a fixed composition. In this case, there is a very small nonmonotonic trend in gas GFE shown in Fig. 2a. The maximum effect of this nonmonotonicity on the interpolated gas relative permeability endpoint is less than 2%. **Fig. 3** shows the sensitivity of GFE and endpoint relative permeability as the concentration of CO_2 is increased from zero to its value at the oil/gas critical point for the same mixture. In this example, the maximum effect

of nonmonotonic behavior in GFE on the endpoint relative permeability is less than 4%, which is less than typical relative permeability measurement errors. None of the test cases for various hydrocarbon mixtures, including multicomponent solvents investigated by Neshat (2016), showed a significant effect of nonmonotonic behavior. However, if calculations for a particular case indicate that there is a significant effect of nonmonotonic behavior, then the method developed by Beygi et al. (2015) that uses both GFE and IFT should be implemented because it is monotonic.

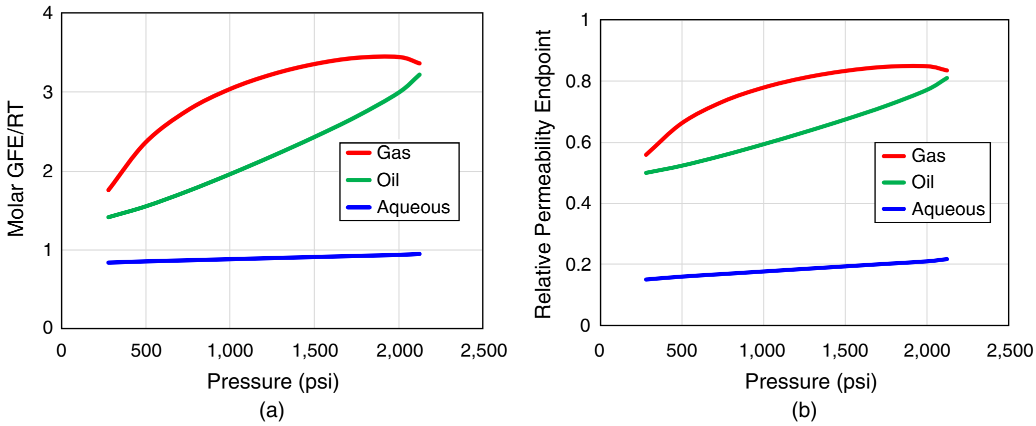

Fig. 2—(a) Molar GFE as a function of pressure for a mixture with composition of 16.67 mol% H_2O, 25 mol% CO_2, 33.3 mol% C_1, and 25 mol% C_6 at 260°F. (b) Endpoint relative permeability interpolated using GFE. The effect of the slight nonmonotonic behavior between 1,900 and 2,100 psia is less than typical experimental uncertainty in relative permeability measurements.

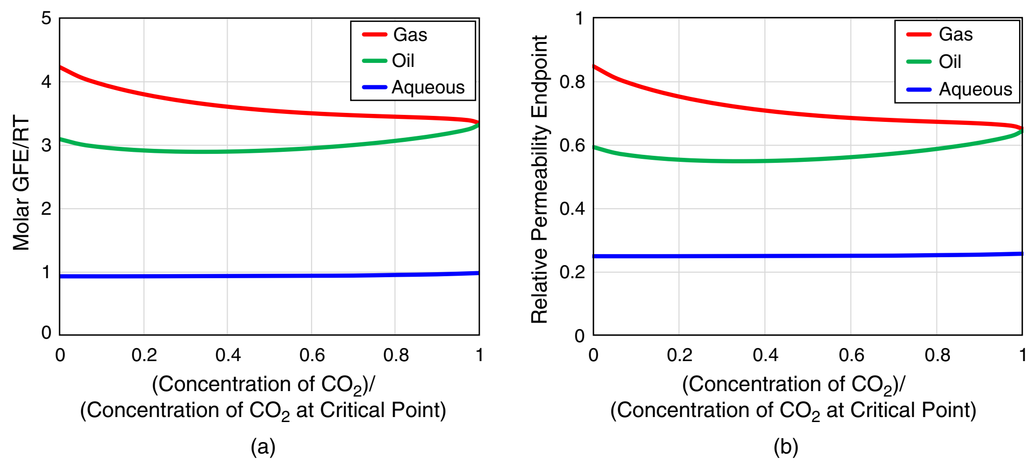

Fig. 3—Molar GFE and interpolated relative permeability endpoints calculated over a wide range of changes in fluid composition. The initial mixture contains 16.7 mol% H_2O, 0 mol% CO_2, 41.65 mol% C_1, and 41.65 mol% C_6. The mole fraction of CO_2 is increased from zero to its value at the oil/gas critical point at 260°, with compositions of 16.7, 35.9, 20.6, and 26.8 mol%. The slight nonmonotonicity in oil GFE has an insignificant effect on endpoint values, which is smaller than typical errors in relative permeability calculations.

Hysteresis. A change in the saturation direction during multiphase flow in porous media results in trapping a portion of the displaced phase by the displacing phase. The volume fraction of the phase trapped, the residual saturation, depends on its maximum historical saturation and can be estimated from the initial residual curve (IRC). Different forms of the Land (1968) equation are commonly used to model the IRC. The modifications usually make use of additional empirical parameters to better match experimental data (Ma and Youngren 1994; Jerauld 1997). For simplicity, the following modified Land (1968) model was used in this study:

$$S_{rj}^{2P} = \frac{S_j^{\max}}{1 + \left(\frac{1}{S_{rj}^{\max}} - 1\right) S_j^{\max\,\frac{1}{1-S_{rj}^{\max}}}} . \quad (3)$$

This correlation guarantees an unconditional slope of zero in the IRC at a saturation of unity, which is known to be consistent with measurements, unlike the original Land (1968) equation (Neshat 2016). $S_{rj}^{\max}$ used in Eq. 3 is calculated by linear interpolation between reference values using GFE (Fig. 1), which ensures compositional consistency in the residual saturations.

The residual saturation from Eq. 3 can be directly applied for hysteretic modeling of two-phase relative permeability. Assuming reversible scanning curves (Braun and Holland 1995), the primary increasing relative permeability curve in conjunction with the saturation at the reversal point can be used to find the two-phase relative permeability in both directions, as shown in **Fig. 4** (Carlson 1981):

$$k_{rj}^{D,I}(S_j) = k_{rj}^{PI}(S_{fj}). \quad (4)$$

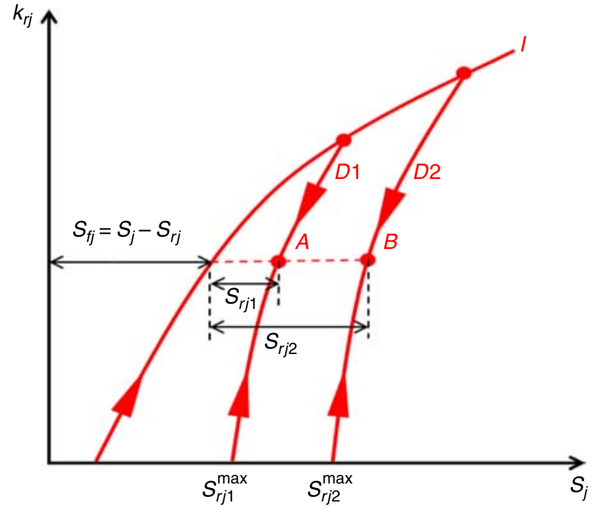

Fig. 4—Primary-increasing and scanning two-phase relative permeability curves.

In Eq. 4 and throughout this paper, *D* and *PI* stand for decreasing- and primary-increasing-saturation directions, respectively. S_{fj} is the flowing saturation of phase *j* calculated from

$$S_{fj}^{2P} = \frac{1}{2}\left[(S_j - S_{rj}^{2P}) + \sqrt{(S_j - S_{rj}^{2P})^2 + \frac{4}{\left(\frac{1}{S_{rj}^{max}} - 1\right)}(S_j - S_{rj}^{2P})}\right]. \quad (5)$$

In three-phase flow, the displacement direction cannot uniquely describe the saturation history because the displacement path is defined by two independent saturations, and an unlimited number of trajectories is possible. **Fig. 5** depicts two different displacement paths, AB and ACB, on a ternary diagram with identical initial and terminal points. Both displacements are identified as IDI processes, where the letters refer to the saturation directions (increasing, decreasing, and increasing) of phases *i, j,* and *k,* respectively. However, taking either of the two paths to get from Point A to Point B would result in a different residual saturation and relative permeability of phase *j* at Point B.

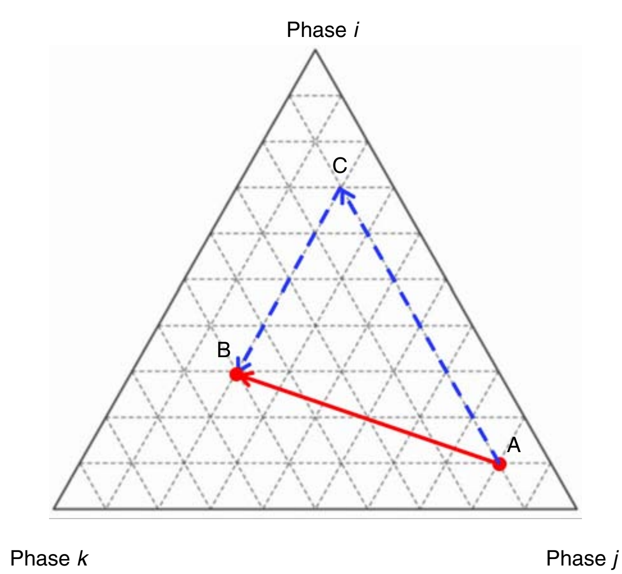

Fig. 5—Alternative saturation-displacement paths in three-phase flow. Paths AB and ACB have the same saturation directions (decreasing S_j) with identical start and endpoints, but the saturation paths are different.

Because experiments with three-phase flow are rare, three-phase relative permeability values are often estimated from data for two-phase flow (Stone 1970, 1973; Baker 1988; Hajilary and Shahmohammadi 2018). This requires a correction to the two-phase residual saturations to include the effect of saturation path. We use the model proposed by Yuan and Pope (2012) for this purpose:

$$S_{rj}^{3P} = \min\left[S_j, S_{rj}^{2P}(1 - b_j S_i S_k)\right]. \quad (6)$$

The expression for three-phase residual saturations can be substituted into Eq. 1 and combined with Eq. 3 for prediction of three-phase relative permeability:

$$k_{rj}^{D}(S_j) = k_{rj}^{0}\left(\frac{S_j - S_{rj}^{3P}}{1 - S_{ri}^{3P} - S_{rk}^{3P}}\right)^{n_j}, \quad (7)$$

where k_{rj}^{0} and n_j are calculated from the primary increasing curve. The new formulation includes the effect of saturation path on three-phase flow using only one parameter (b_j) for each phase. **Fig. 6** shows one example of this model applied for a water-wet Berea sandstone sample. The two-phase primary-increasing data were used as input and the decreasing two- and three-phase relative permeability curves were calculated using Eq. 7. Although the water and gas relative permeability data measured in the increasing and decreasing directions show almost no dependence on the saturation path in two- and three-phase flow (Figs. 6a and 6c), the oil relative permeability data show a significant difference between the two cases (Fig. 6b). The decreasing relative permeability curves are lower than the primary-increasing curve. This constraint is always fulfilled when Eq. 7 is used and eliminates the problem of scanning curves higher than the primary-increasing curve, which sometimes occurs when using relative permeability tables (Kossack 2000). Contours of the three-phase residual saturations at zero relative permeability of each phase are shown in Fig. 6d. In this example, the *b*-parameter for the gas and water phases is zero, consistent with no dependence of the gas and water relative permeability on the saturation path. The *b*-parameter for the oil phase was determined by fitting the model with measured three-phase relative permeability data. However, in the absence of such three-phase data, the *b*-parameter can be estimated using only the residual oil saturation (ROS) to water and the ROS to gas at residual water saturation. Eq. 6 can be solved for *b* using only these two ROS data points, which are nearly always measured.

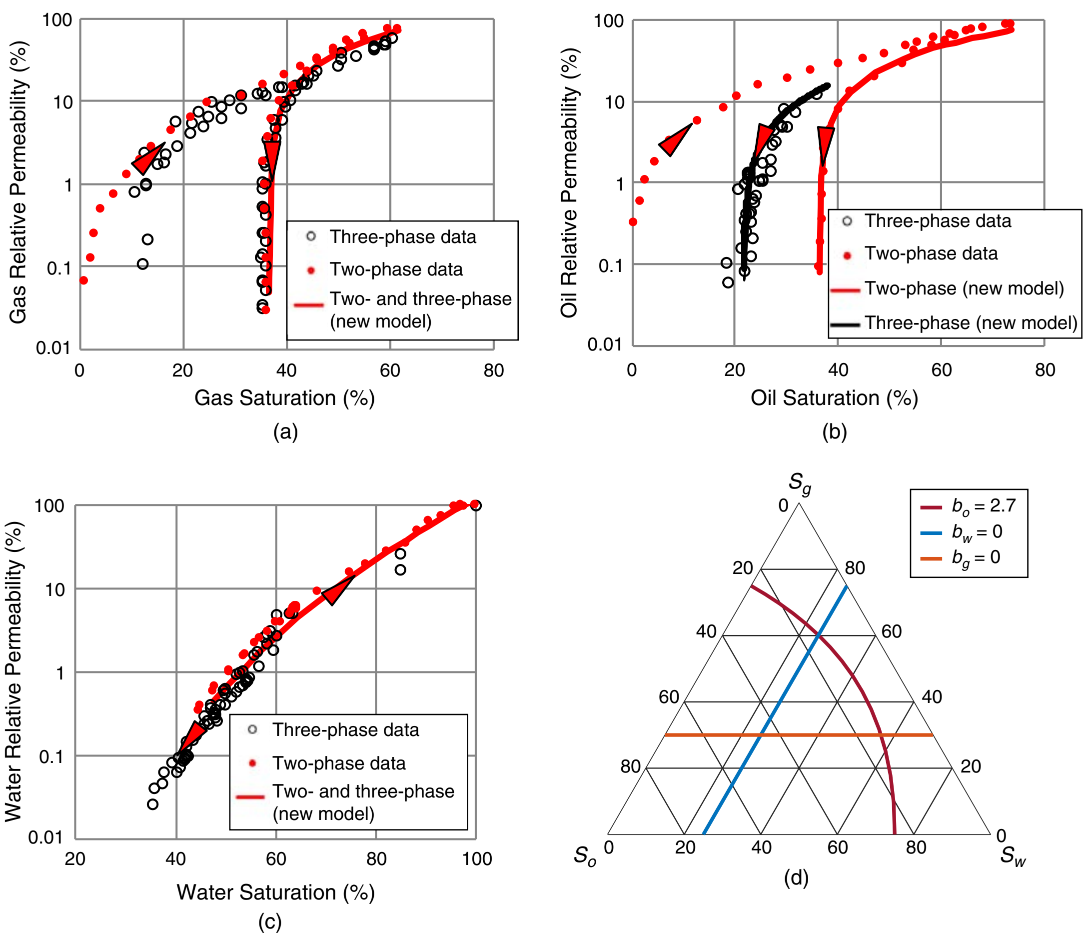

Fig. 6—(a, b, c) Comparison between the calculated relative permeabilities using the new proposed model with measured relative permeability data of gas, oil, and water. The red dots show increasing/decreasing measured data in two-phase displacements and the black circles show measured data in three-phase displacements (Oak et al. 1990). The solid curves show predictions by the proposed model in the decreasing direction using two-phase primary-increasing data as input. (d) Contours of residual saturations of oil, water, and gas at zero relative permeability of each phase.

Scaling Relative Permeability by Trapping Number. The trapping number quantifies the balance of viscous and gravitational forces acting on a phase trapped by capillary forces in a pore throat (i.e., the residual saturation). This dimensionless parameter is evaluated by vector summation of the capillary number and Bond number (Pope et al. 2000) using

$$N_{T_j} = \frac{\left|\overline{\overline{k}} \cdot (\vec{\nabla}\Phi_{j'} + g(\rho_{j'} - \rho_j)\vec{\nabla}D\right|}{\sigma_{jj'}}. \quad (8)$$

The residual saturations are calculated as a function of the trapping number using

$$S_{rj} = \min\left[S_j, S_{rj}^{\text{high}} + \frac{S_{rj}^{\text{low}} - S_{rj}^{\text{high}}}{1 + T_j (N_{T_j})^{\tau_j}}\right]. \quad (9)$$

The endpoint relative permeability and exponent for each phase j are calculated using the residual saturation of phase j':

$$k_{rj}^{0} = k_{rj}^{0\text{ low}} + \frac{S_{rj'}^{\text{low}} - S_{rj'}}{S_{rj'}^{\text{low}} - S_{rj'}^{\text{high}}}\left(k_{rj}^{0\text{ high}} - k_{rj}^{0\text{ low}}\right), \quad (10)$$

$$n_j = n_j^{\text{low}} + \frac{S_{rj'}^{\text{low}} - S_{rj'}}{S_{rj'}^{\text{low}} - S_{rj'}^{\text{high}}}\left(n_j^{\text{high}} - n_j^{\text{low}}\right). \quad (11)$$

Fig. 7 illustrates the dependence of the relative permeability parameters on the trapping number for wetting and nonwetting phases. The corresponding parameters for a third intermediate-wetting phase are between the values for wetting and nonwetting phases. Note that there is no effect of trapping number until it exceeds a critical value, as depicted on the plots.

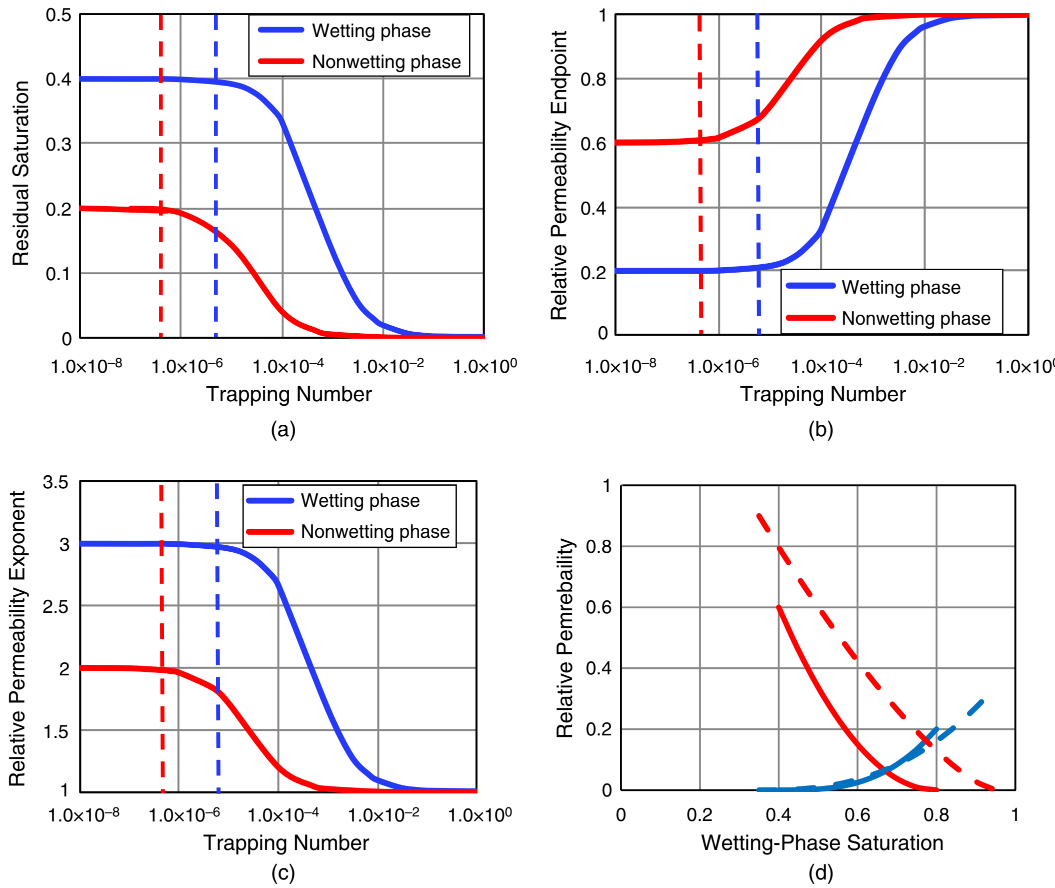

Fig. 7—(a, b, c) Effect of trapping number on wetting-phase (blue) and nonwetting-phase relative permeability parameters; the dashed lines indicate critical trapping numbers. (d) Relative permeability curves at trapping number below the critical value (solid lines) and at a trapping number of 10^{-4} (dashed lines).

Fig. 8 presents a proposed general algorithm for the calculation of relative permeability with hysteresis and trapping-number effects. It should be emphasized that in the new model, all phase-dependent parameters are interpolated between reference values using GFE. This ensures compositional consistency in all steps of the calculations.

Three-Phase Capillary Pressure Model

Capillary pressure and relative permeability are tightly integrated components of multiphase-flow models and should obey consistent principles. Capillary pressure defines the pressure difference existing across the interface between two immiscible phases. In general, capillary pressure is a function of rock wettability, porosity, and permeability, as well as composition and saturation history.

The three-phase capillary pressure model proposed here is derived from a modification and extension of a two-phase model proposed by Skjaeveland et al. (2000). The model is flexible enough to capture the entire range of rock wettability, including mixed-wetting conditions. The generalized form extended to three phases and with permeability and porosity scaling is

$$P_{c,ij} = \sigma_{ij}\cos\theta_{ij}\sqrt{\frac{\phi}{k}}\left[\frac{c_i}{\left(\frac{S_i - S_{ri}}{1 - S_{ri}}\right)^{a_i}} + \frac{c_j}{\left(\frac{S_j - S_{rj}}{1 - S_{rj}}\right)^{a_j}}\right], \quad (12a)$$

$$P_{c,ik} = \sigma_{ij}\cos\theta_{ik}\sqrt{\frac{\phi}{k}}\left[\frac{c_i}{\left(\frac{S_i - S_{ri}}{1 - S_{ri}}\right)^{a_i}} + \frac{c_k}{\left(\frac{S_k - S_{rk}}{1 - S_{rk}}\right)^{a_k}}\right], \quad \text{(12b)}$$

$$P_{c,jk} = \sigma_{ij}\cos\theta_{jk}\sqrt{\frac{\phi}{k}}\left[\frac{c_j}{\left(\frac{S_j - S_{rj}}{1 - S_{rj}}\right)^{a_j}} + \frac{c_k}{\left(\frac{S_k - S_{rk}}{1 - S_{rk}}\right)^{a_k}}\right]. \quad \text{(12c)}$$

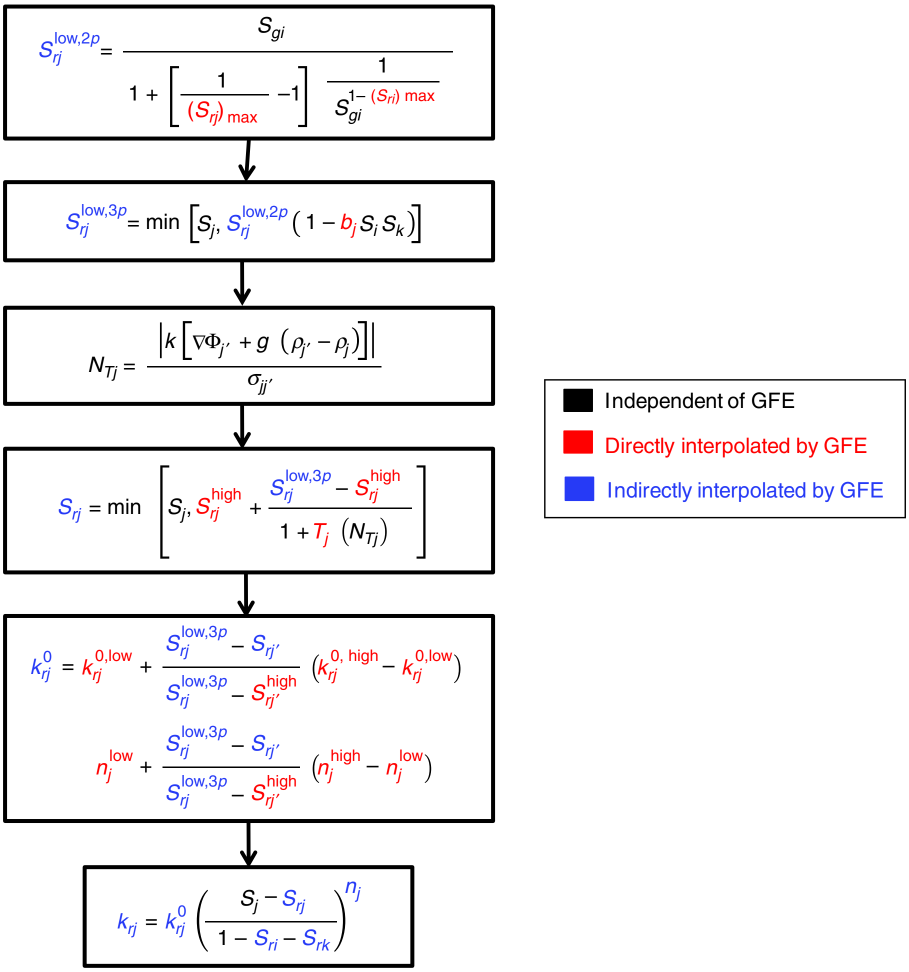

Fig. 8—Flow diagram illustrating the algorithm used to calculate relative permeability with hysteresis and trapping-number effects.

Consistent with the relative permeability model, the residual saturations in Eqs. 12a, 12b, and 12c are calculated from Eq. 5, and the wettability-dependent coefficients a_j and c_j are interpolated using molar GFEs. By definition, the three capillary pressures are related by the constraint

$$P_{c,ij} = P_{c,ik} + P_{c,kj}. \quad \text{(13)}$$

Hence, two capillary pressure values are determined independently from two of the three equations of Eqs. 12a, 12b, and 12c, and the third capillary pressure is defined from Eq. 13. **Fig. 9** shows the phase j primary-increasing surface and the bounding decreasing surface (decreasing surface starting from ultimate residual saturation) of three-phase capillary pressure with residual saturations. Both surfaces are described by Eq. 12a using two independent saturations. However, c_j is set to zero for the primary-increasing surface. All scanning curves resulting from saturation reversal on a primary-increasing surface are expected to lie between the surfaces.

Fig. 10 shows selected contours of constant S_k from the primary increasing, bounding decreasing, and scanning capillary pressure surfaces in Fig. 9. Point R in Fig. 10 indicates a displacement reversal and the corresponding scanning curve started from the primary-increasing curve. To ensure the continuity during transition between the two curves at point R corresponding to $S_j^{\max}$, the following constraint must be satisfied:

$$\frac{c_i}{\left(\frac{S_i^{\max} - S_{ri}}{1 - S_{ri}}\right)^{a_i}} = \frac{c_i}{\left(\frac{S_i^{\max} - S_{ri}^*}{1 - S_{ri}^*}\right)^{a_i}} + \frac{c_j}{\left(\frac{S_j^{\max} - S_{rj}}{1 - S_{rj}}\right)^{a_j}}. \quad \text{(14)}$$

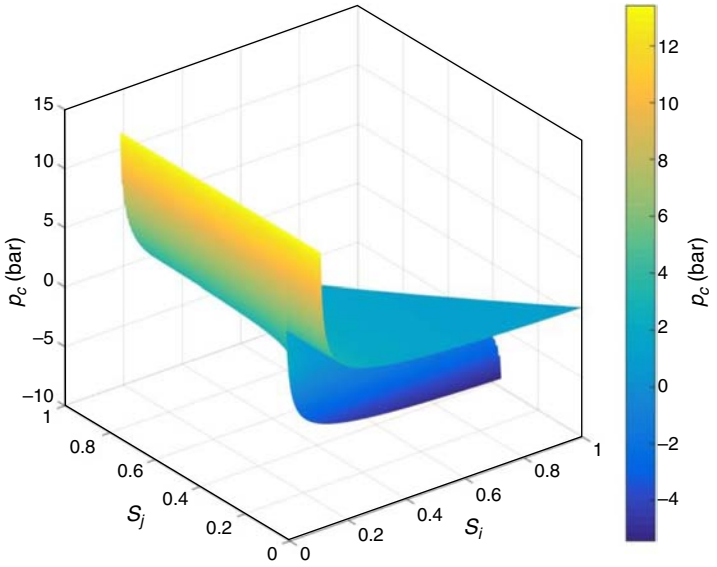

Fig. 9—Surfaces of $P_{c,ij}$ during phase j primary-increasing (top surface) and bounding decreasing (bottom surface) displacements as a function of two independent saturations. The fitting parameters used in Eq. 6 to define three-phase residual saturations are here assumed to be zero ($b_i = b_j = b_k = 0$).

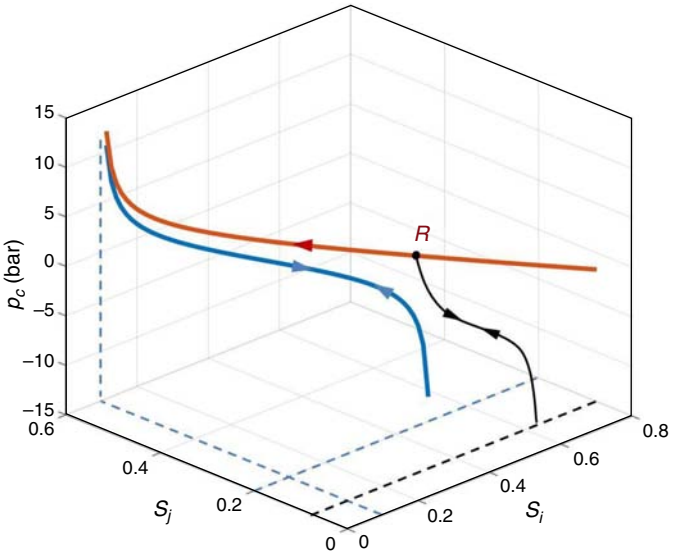

Fig. 10—Primary-increasing (red), bounding decreasing (blue), and scanning (black) $P_{c,ij}$ curves at constant S_k.

S_{rj} and S_{ri} in Eq. 14 are still calculated from Eq. 5. Hence, the only unknown parameter is S^*_{ri}, which is defined by solving Eq. 14. The value of S^*_{ri} approaches S_{ri} as the reversal point becomes close to the residual saturation of phase i. Neshat et al. (2017) used the same type of three-phase capillary pressure function and provided an independent verification of the model by showing good agreement between the model and measured three-phase capillary pressure data.

Selection of Reference Phase. In many reservoir simulators, the oil pressure is by default assumed as the reference pressure. This assumption requires the oil phase to always exist in all parts of the reservoir (all gridblocks in the model reservoir). Hence, it cannot be applied for simulation of gas or gas/condensate reservoirs above the dewpoint, or even oil reservoirs when the oil phase is completely dissolved in some gridblocks because of mass transfer in miscible gasflooding.

In the new GFE model, the choice of reference pressure is dependent on the wettability of the phases, and the most-wetting phase at each gridblock is assumed as the reference pressure. The wettability of the phases can be compared using molar GFEs. One option is to assign the highest wettabilities to the lowest molar GFEs. However, this assumption can be changed depending on the types of rock and fluid. For example, it is also possible to take the phase with intermediate GFE as the most-wetting phase.

Simulation Results

The robustness of the new three-phase relative permeability and capillary pressure models is illustrated by a few challenging simulation examples involving complex phase changes. The new models were implemented in the UTCOMP equation-of-state compositional simulator (Chang 1990; Bang 2007) because it includes three-phase flash and Gibbs-tangent-plane-distance routines. More examples can be found in Neshat (2016).

Enhanced Oil Recovery (EOR) With CO_2/Natural-Gas-Liquid (NGL) Solvent. Solvent miscible flooding is an example of an important EOR process involving complex multicomponent phase behavior. In this example simulation, a seven-component CO_2/NGL solvent is injected and mixes with 12 hydrocarbon components initially in the reservoir (Guler et al. 2001). According to the phase diagram shown in **Fig. 11,** the mixture can split into a maximum of three hydrocarbon phases at different pressures and compositions.

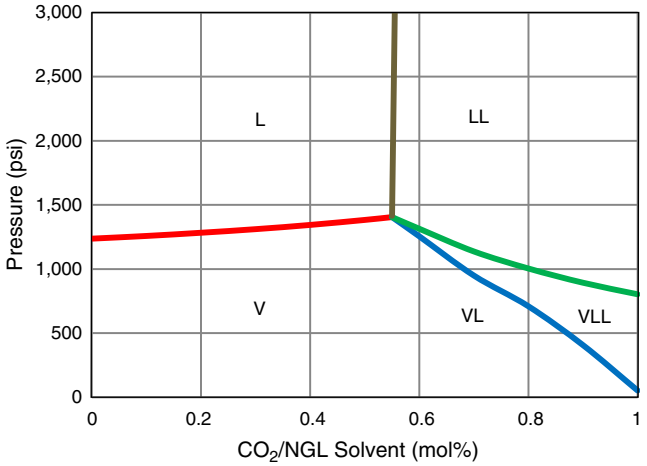

Fig. 11—Pressure vs. composition diagram for the mixture of oil and CO_2/natural-gas-liquid (NGL) solvent. L and V stand for liquid and vapor, respectively.

Figs. 12 and 13 show the results for a 1D simulation. The physical properties are given in **Tables 1 and 2.** The reservoir model is 1,000 ft long, 20 ft wide, and 20 ft thick. The grid is 50×1×1. An injection well is in Gridblock 1, and a production well is in Gridblock 50. Capillary pressure is neglected in this example. Fig. 12a shows a profile of the molar GFE at 120 days. Fig. 1b shows the corresponding saturation and relative permeability profiles. Note that the continuity of the GFE values ensures the continuity of the relative permeability. Fig. 13a shows the trapping-number profile at the same time. The large increase in the trapping number at approximately 500 ft is the result of the low IFT near a critical point. Fig. 13b shows that the trapping number had a significant effect on the relative permeability.

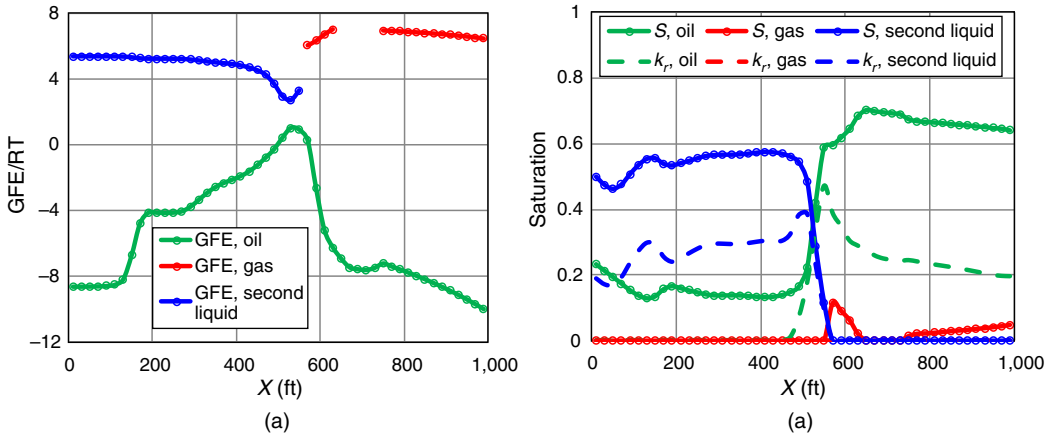

Fig. 12—(a) Molar GFE of hydrocarbon phases and (b) corresponding saturations and relative permeability profiles in 1D reservoir after 120 days.

Fig. 14 shows the results for a 2D homogeneous vertical cross-sectional simulation. The physical properties are identical to the 1D simulation. The reservoir model is 1,000 ft long, 20 ft wide, and 100 ft thick. The grid is 50×1×11. The injection and production wells are perforated in all layers. Fig. 14a shows the GFE of each phase in Layer 6, and Fig. 14b shows the corresponding saturation and relative permeability profiles at 330 days.

Multicycle WAG. WAG is a common method to improve volumetric sweep efficiency. WAG methods can be miscible or immiscible displacements. However, it is sometimes difficult to distinguish between miscibility conditions for WAG injections. In many cases, multicontact gas/oil miscibility might have been obtained, and much uncertainty remains regarding the actual displacement process (Christensen et al. 2001; Hosseininoosheri et al. 2018). Hence, compositional effects should always be considered for more-accurate prediction of this type of recovery process.

A 2D homogeneous vertical cross-sectional reservoir model is used in this example. The physical properties and relative permeability and capillary pressure reference values are given in **Tables 3 through 5.** The reservoir model is 1,000 ft long, 20 ft wide, and 400 ft thick. The grid is 50×10×1. Injection and production wells are perforated in all layers. CO_2 is injected for 15 days, followed by 15 days of water injection during each cycle. The cumulative injection after three cycles is 0.3 pore volumes. **Fig. 15** shows the gas saturation, residual gas saturation, and gas relative permeability for a gridblock at the top of the reservoir adjacent to the injection well. As illustrated in Fig. 15a, the residual gas saturation shows an irreversible increase proportional to its maximum hysteretic saturation. This results in a significant decrease in the gas relative permeability during each new cycle. Fig. 15b shows the three-phase capillary pressure values between oil/gas and oil/water during the three cycles.

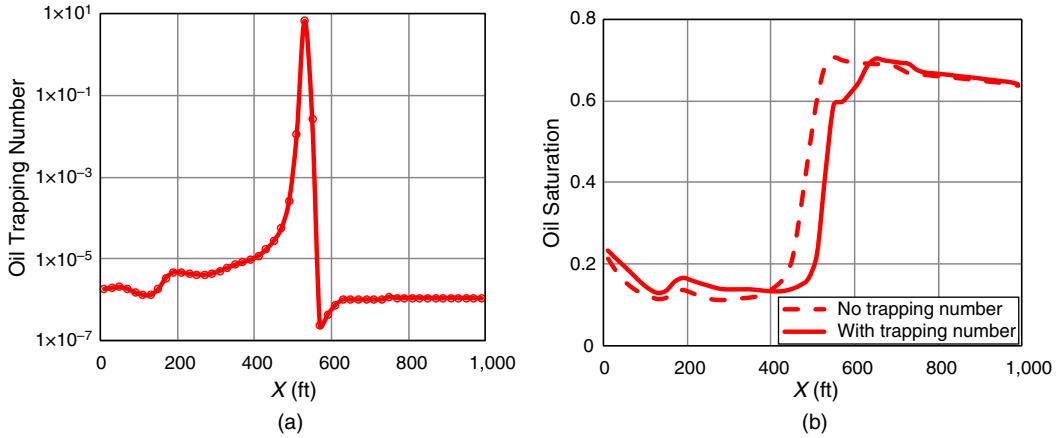

Fig. 13—Profiles of (a) oil trapping number and (b) oil saturation predicted with and without trapping-number effect in 1D reservoir after 120 days.

k_x	137.9 md
k_z	5 md
P (initial)	1,750 psi
Temperature	86°F
Porosity	27.9%
S_w (initial)	40%
Injection pressure	1,800 psi
Production pressure	800 psi

Table 1—Reservoir properties (solvent injection).

	k_r^0	S_r	n	b (Eq. 6)	T (Eq. 9)	GFE/RT
Water	0.1	0.25	3	0.5	1,000	–
Oil	0.5	0.3	2.0	1	20,000	–9.55
Gas	0.9	0.15	3.0	0.5	50,000	5.47
Second liquid	0.7	0.2	2.0	0	30,000	6.94

Table 2—Relative permeability reference values (solvent injection).

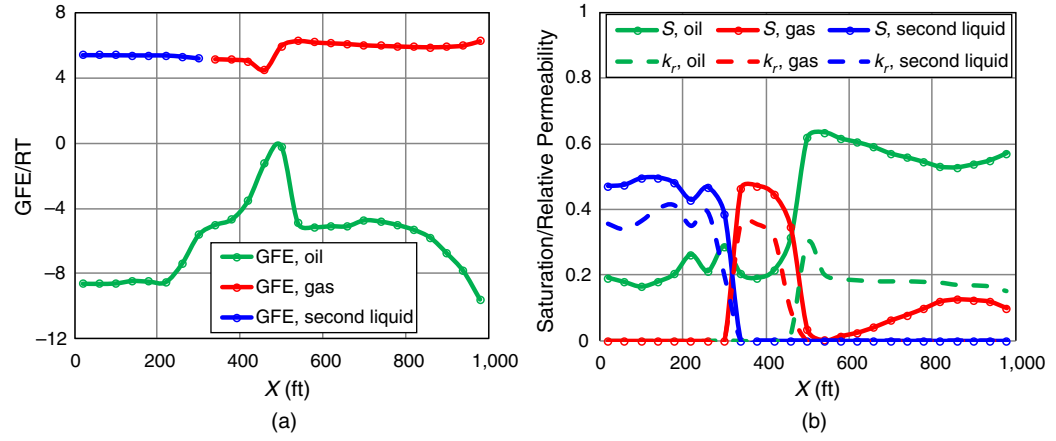

Fig. 14—(a) Molar GFE of hydrocarbon phases and (b) corresponding saturations and relative permeability profiles in 2D reservoir (middle layer) after 330 days.

Length	2,500 ft
Width	50 ft
Thickness	400 ft (1D)
k_x	500 md
k_z	100 md
P (initial)	1,750 psi
Temperature	86°F
Porosity	27.9%
S_w (initial)	40%
Injection pressure	1,800 psi
Production pressure	800 psi

Table 3—Reservoir properties (WAG).

	k_r^0	S_r	n	b (Eq. 6)	T (Eq. 9)	GFE/RT
Water	0.7	0.3	3	0.5	1,000	–
Oil	0.5	0.25	3	1	20,000	–2.7
Gas	0.9	0.35	2	0	40,000	7.4

Table 4—Relative permeability reference values (WAG).

	C_o (psi)	C_g (psi)	C_w (psi)	a_o	a_g	a_w
Water/oil	–2	–	10	2	–	2
Oil/gas	–1	5	–	2	2	–

Table 5—Capillary pressure reference values (WAG).

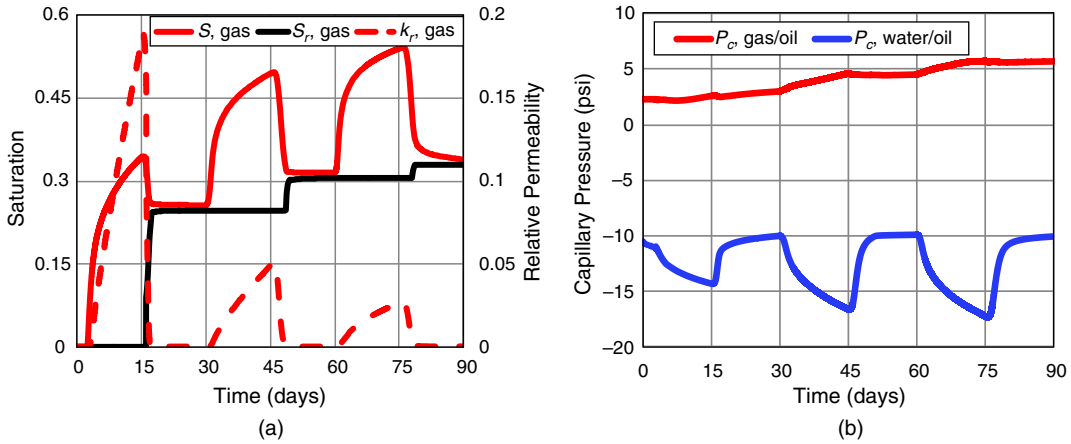

Fig. 15—(a) Saturation, residual saturation, and relative permeability of gas and (b) gas/oil and water/oil capillary pressure in three WAG cycles. All plots belong to a selected cell next to the injection well.

Well Stimulation for Gas/Condensate-Blockage Removal. Gas/condensate buildup around production wells in conventional and unconventional gas reservoirs can have a dramatic effect on production rate because it significantly reduces the gas relative permeability (Pope et al. 2000; Salahshoor and Fahes 2018). Injection of dimethyl ether (DME) into a production well has been proposed as an effective method to remove the water and condensate blockage (Ganjdanesh et al. 2016). When this process was simulated without using the GFE method, frequent phase flipping happened, which caused the timesteps to become very small, and eventually the simulation aborted. This example demonstrates the advantage of applying the GFE method rather than conventional phase-label-dependent models.

A 1D radial homogeneous reservoir with a radius of 2,600 ft and a thickness of 30 ft is modeled in this example. The grid is $50\times1\times1$, with a single well in the center of the grid. Reservoir and grid properties and relative permeability parameters are given in **Tables 6 and 7.** Capillary pressure is neglected in this example. During 50 days of primary production, condensate builds up around the production well. DME is then injected and displaced into the reservoir by N_2 chase gas. **Fig. 16a** shows a snapshot of saturation profiles from simulation output after injection of the chase gas. This plot shows clear discontinuities resulting from phase flipping between aqueous/gas and solvent/gas phases. The saturation profiles with physically correct labels are depicted in Fig. 16b. Although the

misidentification of the phases can make the interpretation of the results difficult, it should be emphasized that this is only a post-processing problem that can be fixed separately. The values of the relative permeability calculated at each timestep in each gridblock during the simulation are unconditionally continuous when the GFE model is used. Therefore, the calculated values for relative permeability are inherently correct, even if erroneous labels are assigned in the output. This completely solves the problems of phase flipping and discontinuities in flux calculations. **Fig. 17** shows the profiles of relative permeability from simulation before and after correcting the phase labels. **Fig. 18** shows the change in relative permeability caused by the DME treatment and the resulting increase in production rate from the condensate reservoir.

k_x	10 md
P (initial)	2,000 psi
Temperature	100°F
Porosity	16%
S_w (initial)	70%
Production pressure	1,000 psi

Table 6—Reservoir properties (DME injection).

	k_r^0	S_r	n	b (Eq. 5)	T (Eq. 7)	GFE/RT
Oil	0.5	0.3	3.0	1	20,000	1.82
Gas	0.85	0.2	2.0	0	50,000	8.65
Aqueous	0.15	0.25	2.0	0	2,000	2.72

Table 7—Relative permeability reference values (DME injection).

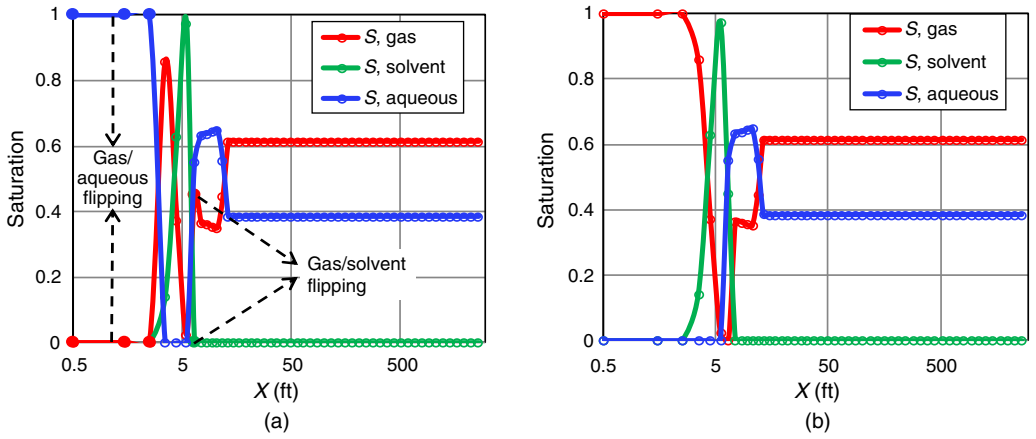

Fig. 16—Saturation profiles after injection of chase gas: (a) simulation output before correcting phase labels; (b) after correcting phase labels. The flipping phases are marked by filled circles.

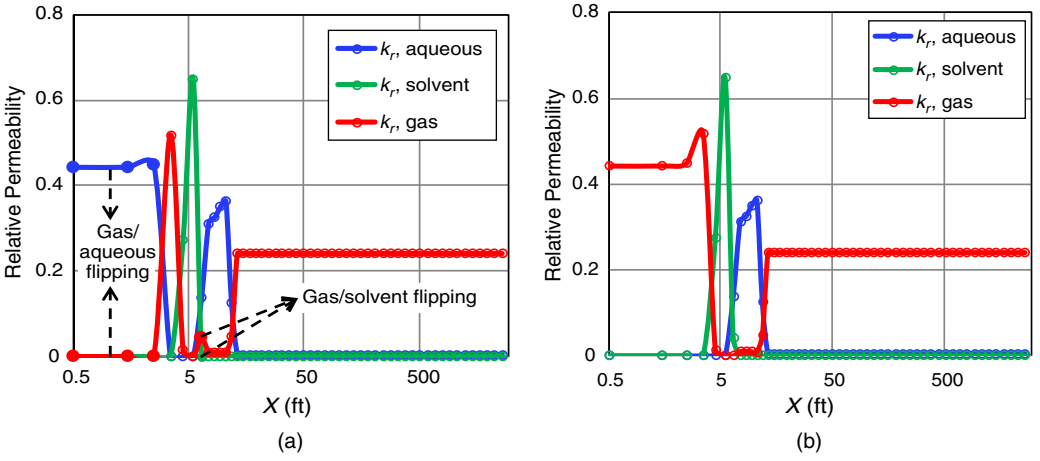

Fig. 17—Relative permeability profiles after injection of chase gas (a) calculated from erroneous phase labels and (b) predicted by the new model unaffected by erroneous phase labels. The flipping phases are marked by filled circles.

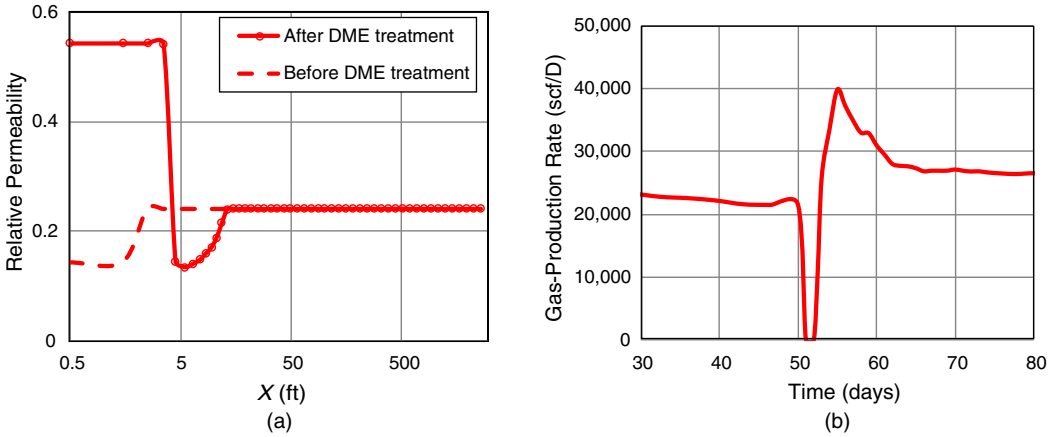

Fig. 18—(a) Contours of gas relative permeability before and after DME treatment; (b) gas-production rate.

Conclusions

New coupled three-phase relative permeability and capillary pressure models have been developed and tested for use in compositional reservoir simulators. The effects of hysteresis on two- and three-phase displacements were incorporated into the models. The Carlson (1981) method was modified to capture the effect of saturation direction. A new and simple approach was introduced to include the effect of a saturation path using only one empirical parameter. The new three-phase hysteresis model is in good agreement with three-phase relative permeability experimental data used in this study. The relative permeability parameters and residual saturations are a function of trapping number. A new general three-phase capillary pressure model was developed that can be applied for all wettability conditions and pore structures. The parameters in the new hysteretic capillary pressure model were interpolated with GFE to ensure compositional continuity.

Using GFE as a measure of phase composition offers significant advantages over conventional models. First, it ensures compositional consistency during phase changes. Second, relative permeability and capillary pressure parameters are evaluated independent of phase labels, and consequently are not affected by phase misidentification or flipping. Most importantly, the GFE model captures the effect of composition on relative permeability that has been observed experimentally. The new models were used for the hysteretic simulation of recovery processes, such as solvent flooding, multicycle WAG, and well stimulation. Numerical stability, consistency of numerical results with known physics of capillary pressure and relative permeability behavior, and reduced computational time are among the advantages of using the new coupled models.

Nomenclature

a_j = capillary pressure exponent of phase j
b_j = adjustable parameter for phase j three-phase residual saturation
c_j = capillary entry pressure of phase j, m/Lt^2, psi
D = depth, L, ft
g = acceleration of gravity, L/t^2, ft/sec^2
G_j = molar Gibbs free energy of phase j, mL^2/t^{2}N, Btu/lb-mol
k = permeability in horizontal direction, L^2, md
k_{rj} = relative permeability of phase j
k^0_{rj} = endpoint relative permeability of phase j
$\overline{\overline{k}}$ = permeability tensor, L^2, md
n_j = relative permeability endpoint of phase j
N_{T_j} = trapping number of phase j
$P_{c,ij}$ = capillary pressure between phases i and j, m/Lt^2, psi
R = gas constant, mL^2/t^{2}NT, psia-ft^3/lb-mol-°R
S_{fj} = flowing saturation of phase j
S_j = saturation of phase j
$S_j^{\max}$ = maximum hysteretic saturation of phase j
S_{rj} = residual saturation of phase j
$S_{rj}^{\max}$ = maximum residual saturation of phase j defined from IRC
S^*_{rj} = reversal saturation parameter for phase j (Eq. 14)
T = temperature, T, °F
T_j = trapping parameter for phase j
θ_{ij} = contact angle between phases i and j
ρ_j = density of phase j, m/L^3, lbm/ft^3
σ_{ij} = IFT between phases i and j, m/t^2, dyne/cm
τ_j = trapping exponent for phase j
ϕ = porosity
Φ = fugacity coefficient
Φ_j = potential of phase j, mL^2/t^2, Btu

Superscripts

D = decreasing saturation
high = high trapping number

I = increasing saturation
low = low trapping number
PI = primary-increasing saturation
$2P$ = two-phase
$3P$ = three-phase

Subscripts

f = flowing
i, j, k = phase indicators
j' = conjugate phase displaced by displacing phase j
n = component indicator
r = residual

References

Alzayer, A., Voskov, D., and Tchelepi, H. 2016. On Modification of Relative Permeability in Compositional Simulation of Near-Miscible Processes. Oral presentation given at ECMOR XV–15th European Conference on the Mathematics of Oil Recovery, Amsterdam, 29 August–1 September.

Baker, L. E. 1988. Three-Phase Relative Permeability Correlations. Presented at the SPE Enhanced Oil Recovery Symposium, Tulsa, 16–21 April. SPE-17369-MS. https://doi.org/10.2118/17369-MS.

Bang, V. 2007. *Development of a Successful Chemical Treatment for Gas Well With Condensate or Water Blockage Damage*. PhD dissertation, University of Texas at Austin, Austin, Texas.

Beygi, M. R., Delshad, M., Pudugramam, V. S. et al. 2015. Novel Three-Phase Compositional Relative Permeability and Three-Phase Hysteresis Models. *SPE J.* **20** (1): 21–34. SPE-165324-PA. https://doi.org/10.2118/165324-PA.

Blunt, M. J. 2000. An Empirical Model for Three-Phase Relative Permeability. *SPE J.* **5** (4): 435–445. SPE-67950-PA. https://doi.org/10.2118/67950-PA.

Braun, E. M. and Holland, R. F. 1995. Relative Permeability Hysteresis: Laboratory Measurements and a Conceptual Model. *SPE J.* **10** (3): 222–228. SPE-28615-PA. https://doi.org/10.2118/28615-PA.

Brooks, R. H. and Corey, A. T. 1966. Hydraulic Properties of Porous Media Affecting Fluid Flow. *J. Irrig. Drain. Div.* **92** (2): 61–90.

Carlson, F. M. 1981. Simulation of Relative Permeability Hysteresis to the Non-Wetting Phase. Presented at the SPE Annual Technical Conference and Exhibition, San Antonio, Texas, 4–7 October. SPE-10157-MS. https://doi.org/10.2118/10157-MS.

Chang, Y. 1990. *Development and Application of an Equation of State Compositional Simulator*. PhD dissertation, University of Texas at Austin, Austin, Texas.

Chen, X. 2016. *Experimental Studies on CO_2-Brine-Decane Relative Permeabilities in Berea Sandstone With New Steady-State and Unsteady-State Methods*. PhD dissertation, University of Texas at Austin, Austin, Texas.

Christensen, J. R., Stenby, E. H., and Skauge, A. 2001. Review of WAG Field Experience. *SPE Res Eval & Eng* **4** (2): 97–106. SPE-71203-PA. https://doi.org/10.2118/71203-PA.

Corey, A. T., Rathjens, C. H., Henderson, J. H. et al. 1956. Three-Phase Relative Permeability. *J Pet Technol* **8** (11): 63–65. SPE-737-G. https://doi.org/10.2118/737-G.

Dria, D. E., Pope, G. A., and Sepehrnoori, K. 1993. Three-Phase Gas/Oil/Brine Relative Permeabilities Measured Under CO_2 Flooding Conditions. *SPE Res Eng* **8** (2): 143–150. SPE-20184-PA. https://doi.org/10.2118/20184-PA.

Fayers, F. J., Foakes, A. P., Lin, C. Y. et al. 2000. An Improved Three-Phase Flow Model Incorporating Compositional Variance. Presented at the SPE/DOE Improved Oil Recovery Symposium, Tulsa, 2–5 April. SPE-59313-MS. https://doi.org/10.2118/59313-MS.

Ganjdanesh, R., Rezaveisi, R. Pope, G. A. et al. 2016. Treatment of Condensate and Water Blocks in Hydraulic-Fractured Shale-Gas/Condensate Reservoirs. *SPE J.* **21** (2): 665–674. SPE-175145-PA. https://doi.org/10.2118/175145-PA.

Guler, B., Wang, P., Delshad, M. et al. 2001. Three- and Four-Phase Flow Compositional Simulations of CO_2/NGL EOR. Presented at the SPE Annual Technical Conference and Exhibition, New Orleans, 30 September–3 October. SPE-71485-MS. https://doi.org/10.2118/71485-MS.

Hajilary, N. and Shahmohammadi, A. 2018. New Permeability Model for Gel Coated Porous Media With Radial Flow. *J. Appl. Fluid Mech.* **11** (2): 397–404. https://doi.org/10.18869/acadpub.jafm.73.245.27874.

Hosseininoosheri, P., Hosseini, S. A., Nuñez-López, V. et al. 2018. Impact of Field Development Strategies on CO_2 Trapping Mechanisms in a CO_2-EOR Field: A Case Study in the Permian Basin (SACROC Unit). *Int. J. Greenh. Gas Contr.* **72** (May): 92–104. https://doi.org/10.1016/j.ijggc.2018.03.002

Jerauld, G. R. 1997. General Three-Phase Relative Permeability Model for Prudhoe Bay. *SPE Res Eng* **12** (4): 255–263. SPE-36178-PA. https://doi.org/10.2118/36178-PA.

Jordan, P. B. 2016. *Two-Phase Relative Permeability Measurements in Berea Sandstone at Reservoir Conditions*. Master's thesis, University of Texas at Austin, Austin, Texas.

Kalla, S., Leonardi, S. A., Berry, D. W. et al. 2015. Factors That Affect Gas-Condensate Relative Permeability. *SPE J.* **18** (1): 5–10. SPE-173177-PA. https://doi.org/10.2118/173177-PA.

Kossack, C. A. 2000. Comparison of Reservoir Simulation Hysteresis Options. Presented at SPE Annual Technical Conference and Exhibition, Dallas, 1–4 October. SPE-63147-MS. https://doi.org/10.2118/63147-MS.

Land, C. S. 1968. Calculation of Imbibition Relative Permeability for Two- and Three-Phase Flow From Rock Properties. *SPE J.* **8** (2): 149–156. SPE-1942-PA. https://doi.org/10.2118/1942-PA.

Larsen, J. A. and Skauge, A. 1998. Methodology for Numerical Simulation With Cycle-Dependent Relative Permeabilities. *SPE J.* **3** (2): SPE-38456-PA. https://doi.org/10.2118/38456-PA.

Ma, T. D. and Youngren, G. K. 1994. Performance of Immiscible Water-Alternating-Gas (IWAG) Injection at Kuparuk River Unit, North Slope, Alaska. Presented at the SPE Annual Technical Conference and Exhibition, New Orleans, 25–28 September. SPE-28602-MS. https://doi.org/10.2118/28602-MS.

Muskat, M. 1949. *Physical Principles of Oil Production*. New York City: McGraw-Hill.

Neshat, S. S. 2016. *Compositional Three-Phase Relative Permeability and Capillary Pressure Models Using Gibbs Free Energy*. Master's thesis, University of Texas at Austin, Austin, Texas.

Neshat, S. S., Okuno, R., and Pope, G. A. 2017. A Rigorous Solution to the Problem of Phase Behavior in Unconventional Formations With High Capillary Pressure. Presented at the SPE Annual Technical Conference and Exhibition, San Antonio, Texas, 9–11 October. SPE-187260-MS. https://doi.org/10.2118/187260-MS.

Oak, M. J., Baker, L. E., and Thomas, D. C. 1990. Three-Phase Relative Permeability of Berea Sandstone. *J Pet Technol* **42** (8): 1054–1061. SPE-17370-PA. https://doi.org/10.2118/17370-PA.

Pope, G. A., Wu, W., Narayanaswamy, G. et al. 2000. Modeling Relative Permeability Effects in Gas-Condensate Reservoirs With a New Trapping Model. *SPE Res Eval & Eng* **3** (2): 171–178. SPE-62497-PA. https://doi.org/10.2118/62497-PA.

Salahshoor, S. and Fahes, M. 2018. Experimental Determination of the Phase Transition Point in Gas Condensate Using a Cost-Effective Semiautomated Isochoric Apparatus. Presented at the SPE Western Regional Meeting, Garden Grove, California, 22–26 April. SPE-190102-MS. https://doi.org/10.2118/190102-MS.

Skjaeveland, S. M., Siqveland, L. M., Kjosavik, A. et al. 2000. Capillary Pressure Correlation for Mixed-Wet Reservoirs. *SPE J.* **3** (1): 60–67. SPE-60900-PA. https://doi.org/10.2118/60900-PA.

Stone, H. 1970. Probability Model for Estimating Three-Phase Relative Permeability. *J Pet Technol* **22** (2): 214–218. SPE-2116-PA. https://doi.org/10.2118/2116-PA.

Stone, H. L. 1973. Estimation of Three-Phase Relative Permeability and Residual Oil Data. *J Can Pet Technol* **12** (4): 214–218. PETSOC-73-04-06. https://doi.org/10.2118/73-04-06.

Yuan, C. and Pope, G. 2012. A New Method to Model Relative Permeability in Compositional Simulators To Avoid Discontinuous Changes Caused by Phase Identification Problems. *SPE J.* **17** (4): 1221–1230. SPE-142093-PA. https://doi.org/10.2118/142093-PA.

Sajjad S. Neshat is a PhD degree candidate at the University of Texas at Austin. His research interests include thermodynamics and phase behavior of reservoir fluids, modeling multiphase flow in porous media, compositional reservoir simulations, and data analysis. Neshat holds two bachelor's degrees in petroleum engineering and mechanical engineering, both from Sharif University of Technology, Iran, and a master's degree in mechanical engineering from the University of Texas at Austin.

Gary A. Pope is a professor in the Hildebrand Department of Petroleum and Geosystems Engineering at the University of Texas at Austin, where he holds the Texaco Centennial Chair in Petroleum Engineering. His teaching and research are in the areas of EOR, reservoir engineering, natural-gas engineering, and reservoir simulation. Pope holds a bachelor's degree from Oklahoma State University and a PhD degree from Rice University, both in chemical engineering. He was elected to the National Academy of Engineering in 1999. Pope is an SPE Honorary Member and an SPE Distinguished Member. His awards include the AIME Environmental Conservation Distinguished Service Award, the Billy and Claude R. Hocott Distinguished Centennial Engineering Research Award, the SPE IOR Pioneer Award, the SPE/AIME Anthony F. Lucas Gold Medal, the SPE John Franklin Carll Award, the SPE Distinguished Achievement Award, and the SPE Reservoir Engineering Award.